PHYSICAL REVIEW B VOLUME 25, NUMBER 2 15 JANUARY 1982

Diffuse scattering from dislocation loops

P. Ehrhart* and H. Trinkaus
Institut für Festkörperforschung der Kernforschungsanlage Jülich, Postfach 1913, D-5170 Jülich, Germany

B. C. Larson
Solid State Division, Oak Ridge National Laboratory, Oak Ridge, Tennessee 37830
(Received 26 January 1981)

Diffuse scattering from crystals containing dislocation loops has been calculated. An emphasis was made to reduce numerical computation of lattice sums by an appropriate summing procedure and by limitation of the summation volume by a smooth damping function. The fundamental details of the scattering pattern are discussed in relation to various analytical schemes. Detailed examples are given for circular loops on {111} planes in an elastically isotropic fcc crystal. Characteristic differences are shown between perfect and faulted loops and between vacancy- and interstitial-type loops. Procedures for quantitative determination of loop sizes and concentrations are discussed.

I. INTRODUCTION

For many high-energy-particle irradiation and thermal-annealing conditions in metals, the primary irradiation defects (i.e., vacancies and interstitials) condense into dislocation loops that are stable up to rather high temperatures (>600 K). The number density and the detailed structure of these loops are of fundamental interest for the understanding of the mechanical behavior of irradiated metals.

The dominant method for the investigation of these loops has been the electron microscope, which yields direct information on individual loops. On the other hand, it has been quite tedious and difficult to routinely investigate sufficiently large numbers of defects to provide statistically reliable information simultaneously on the number, size, orientation, and vacancy-interstitial nature of loops present in a sample using the electron microscope. For smaller-sized loops where the resolution of the microscope becomes important, this is especially true.

Diffuse scattering of x rays has been successfully used for the detailed investigation of smaller-sized defects[1] and can be used as a method to obtain average defect parameters for a distribution of larger-sized defects as well. Considerable progress has been achieved in this area during the last 20 years as discussed in a recent review.[2] At present, the experimental techniques are rather well developed, and with the added availability of synchrotron radiation for diffuse-scattering measurements, very detailed measurements will be possible.

For reliable quantitative evaluations of these measurements, however, accurate and routinely available calculational methods need to be provided. Exact analytical expressions have been given for the scattering very close to Bragg reflections.[3,4] For the scattering at larger distances approximations yield only the qualitative behavior of the scattering.[4–7] However, for quantitative analyses of diffuse-scattering data, numerical calculations are necessary.[8,9] Although general expressions have been available for numerical calculations of the scattering from dislocation loops using the strain field surrounding the loops, straightforward calculations have proved to be very time consuming, even on the largest computers.[8]

This work was undertaken to improve both the computational techniques and the analytical understanding of the scattering characteristics. Because of the complicated nature of the strain field, no single analytic or numerical approach can be used to evaluate the scattering for all regions of reciprocal space. Rather, the scattering has been considered in terms of the Huang diffuse scattering (HDS) from the long-range part of the strain field, asymptotic diffuse scattering (ADS) from the highly strained region in the close vicinity of the loop plane, and structural diffuse scattering (SDS) from the atomistic crystal-structure stacking sequence and the core of the dislocation loop.

In the following section the basic scattering

equation is introduced. In Sec. III we show the numerical methods that have been used to overcome the problems connected with the slow convergence of the lattice sums and the corresponding large computer times. In Sec. IV we will show how the most characteristic features of the scattering pattern can be derived from an analytical study of its zeros and maxima. The relevance of these results for the interpretation of the numerical calculations is demonstrated at some specially oriented loops. In Sec. V a more detailed set of results is shown for circular loops on the close-packed {111} planes in an elastically isotropic fcc lattice. For all numerical examples the lattice spacing $a=4.04$ Å and the Poisson ratio $\nu=0.347$ of aluminium are taken for which elastic isotropy is a good approximation. Elastic anisotropy does not change the basic features of the scattering. Its quantitative influence will be discussed in a subsequent paper.

II. SCATTERING EQUATION

In the kinematic theory of diffraction, the diffuse-scattering *intensity* arising from a small concentration of randomly distributed lattice defects is obtained by the incoherent summation of the contributions from each defect. The scattering *amplitude* of the individual defects is given by a coherent superposition of the scattering amplitudes resulting from the defect atoms and the displaced lattice atoms in their neighborhood. Accordingly, in units of a single lattice atom, the diffuse-scattering intensity arising from a dislocation loop may be written as[3-7]

$$I=\left|\sum_m e^{i\vec{K}\cdot\vec{r}_m}(e^{i\vec{K}\cdot\vec{s}_m}-1)\pm\sum_n e^{i\vec{K}\cdot(\vec{r}_n+\vec{s}_n)}\right|^2. \tag{1a}$$

The first sum in Eq. (1a) describes the diffuse-scattering amplitude (total amplitude minus the Bragg reflection amplitude) from the lattice atoms m displaced from their ideal positions $\vec{r}_m$ by $\vec{s}_m$ due to the presence of the dislocation loop ("distortion scattering"). The second sum represents the scattering amplitude from the additional or missing atoms n, which define the lattice defect ("Laue scattering"). $\vec{K}$ is the scattering vector.

The distortion scattering and the Laue scattering are essentially different in character. Since the (long-range) displacement field of a dislocation loop is smoothly varying in the lattice, the distortion scattering is concentrated in the regions $|\vec{q}|=|\vec{K}-\vec{G}|\lesssim G\epsilon\simeq Gb/R$ around the reciprocal-lattice points where $\epsilon\sim b/R$ gives the order of the strains in the region (for example, in the center) of a dislocation loop of Burger's vector b and radius R. In contrast to this, the Laue scattering arising from disorder on an atomic scale is spread out over reciprocal space.

A basic assumption underlying Eq. (1a) is that the dislocation loops are *randomly* distributed. Accordingly, the considerations in this paper are restricted to crystals with small loop concentrations (loop separation large compared with loop diameter), for which correlations or intersections of loops may be neglected.

III. NUMERICAL METHODS

As the displacement field $\vec{s}$ of a dislocation loop can be calculated by elastic continuum theory,[10] the scattering can be calculated in a straightforward manner by the use of Eq. (1a). Because of the slow $1/r^2$ decrease of the displacements, the convergence of the sum is very poor and, consequently, a very large number of atoms must be considered.[8] Therefore, it was necessary to reduce the number of actual summation steps drastically.

A. Use of periodicity and symmetry

Using the periodicity of the lattice we can rewrite Eq. (1a) as

$$I=\left|\sum_m e^{i\vec{q}\cdot\vec{r}_m}(e^{i\vec{K}\cdot\vec{s}_m}-1)+L\right|^2, \tag{1b}$$

where L indicates the Laue scattering.

If we are mainly interested in the scattering close to Bragg reflections, this formula has the advantage that the phase factors ($e^{i\vec{q}\cdot\vec{r}_m}$) are identical for different Bragg reflections. However, it must be remembered that the phase factor $\Phi=e^{i\vec{G}\cdot\vec{r}_m}$ is, in general, not equal to 1 if the center of the loop is considered to be the origin of the lattice. For an intrinsic defect like a vacancy loop, $\Phi=1$ always, but for extrinsic interstitial loops, $\Phi=1$ for even reflections; for odd reflections, $\Phi=-1$ because the distance from the loop plane to the first neighboring lattice plane is only half a lattice translation vector.
summation in Eqs. (1a) and (1b) is necessary only over half of the lattice volume $V/2$, and only the real part of the sum must be considered so that

$$I=\left|2\sum_{V/2}\{\cos(\vec{q}\cdot\vec{r})[\cos(\vec{K}\cdot\vec{s})-1]-\sin(\vec{q}\cdot\vec{r})\sin(\vec{K}\cdot\vec{s})\}+L\right|^2. \tag{2a}$$

Thus the lattice sum can be split into a symmetric and an antisymmetric part with respect to $\vec{q}$ and $\vec{s}$.

For calculations of the scattering intensity around Bragg reflections, the scattering vector may be further divided into ($\vec{K}=\vec{G}+\vec{q}$):

$$I=\left|2\sum_{V/2}\{\cos(\vec{q}\cdot\vec{r})[\cos(\vec{q}\cdot\vec{s})\cos(\vec{G}\cdot\vec{s})-\sin(\vec{q}\cdot\vec{s})\sin(\vec{G}\cdot\vec{s})-1]\right.$$
$$\left.-\sin(\vec{q}\cdot\vec{r})[\sin(\vec{q}\cdot\vec{s})\cos(\vec{G}\cdot\vec{s})+\cos(\vec{q}\cdot\vec{s})\sin(\vec{G}\cdot\vec{s})\}+L\right|^2. \tag{2b}$$

Thus intensities at points $\vec{q}$ and $\vec{q}'=-\vec{q}$ can be evaluated with one set of trigonometric functions.

B. Convergence of the lattice sum

In order to limit computer time the lattice sum must be confined someway. Since a sharp truncation of the sum results in spurious ripples in the intensity distribution, a smoothly decaying function should be used as has been discussed by Keating and Goland.[11] Accordingly, we have introduced a Gaussian function $\exp[-(1/2d^2)r^2]$ to Eq. (2). Mathematically, this is related to a convolution of the intensity distribution $I(q)$ with a Gaussian function $\exp(-\frac{1}{2}d^2q^2)$. The corresponding smearing out of the intensity distribution can be kept negligible compared to the resolution of the experiments, and still results in significant computational savings. Values of $d\simeq 2$ to 3 times the loop radius (R) were found to be reasonable values for 20-Å loops as discussed below.

For small values of q ($qR<3$) this method cannot be applied (or only with a much broader Gaussian, which would no longer be effective in reducing the integration volume). For this region of q the convergence of the sum was improved by subtracting $\vec{K}\cdot\vec{s}$ under the sum of Eqs. (2) [i.e., the leading term of the expansion of $\exp(i\vec{K}\cdot\vec{s})$] and correcting this[12] by adding

$$\vec{K}\cdot\vec{s}^{\,*}(\vec{q})=\sum_m e^{i\vec{q}\cdot\vec{r}_m}\vec{K}\cdot\vec{s}_m$$
$$\sim\frac{1}{v}\int dV e^{i\vec{q}\cdot\vec{r}}\vec{K}\cdot\vec{s}(\vec{r}),$$

where v is the atomic volume. Then, Eq. (2a) becomes

$$I=\left|2\sum_{V/2}\{\cos(\vec{q}\cdot\vec{r})[\cos(\vec{K}\cdot\vec{s})-1]\right.$$
$$-\sin(\vec{q}\cdot\vec{r})[\sin(\vec{K}\cdot\vec{s})-\vec{K}\cdot\vec{s}_m]\}$$
$$\left.+\vec{K}\cdot\vec{s}^{\,*}(\vec{q})+L\right|^2. \tag{2c}$$

In addition, a considerable amount of calculation time can be saved by calculating the trigonometric functions for equally spaced distances in reciprocal space as shown by Keating and Goland.[8]

A further reduction of calculation time was achieved by the introduction of a structure factor F_1 that sums the scattering amplitude from many atoms at larger distances from the loop. Therefore, the integration volume was divided into cubes of varying sizes for different distances from the loop. In the innermost regions ($r\lesssim 3R$) the calculations were done completely atomistically according to Eqs. (2a) and (2b). For the next inner shell, 12 atoms were summed in a unit cell with a structure factor F_1. This particular unit cell was chosen for convenience to get a simple lattice. For the succeeding areas the dimensions of the unit cell were increased by a factor of 2 in each direction yielding 96, 768, and 6144 atoms per cell, respectively. The unit cell of the second region of the integration volume is shown in Fig. 1 as an example of an fcc lattice in which the three (111) planes corresponding to the A, B, and C stacking sequences are indicated by different symbols. In order to obtain a cell with inversion symmetry and, consequently, a real structure factor

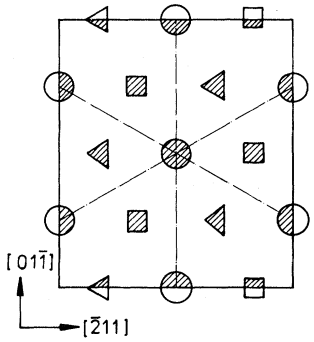

FIG. 1. Projection on the (111) plane of a unit cell containing 12 atoms of the fcc lattice. The three different stacking planes (A, B, and C) are indicated by different symbols.

$F_1 = \sum_{V_c} e^{i\vec{K}\cdot\vec{r}} = \sum_{V_c} \cos(\vec{K}\cdot\vec{r})$, the atoms at the border of the cells are shared between the neighboring cells. Doing the summation of Eq. (2) over such cells instead of individual atoms corresponds to neglecting the change in the lattice displacements $\vec{s}(\vec{r})$ within the cells. However, for larger distances, the change in the displacements is small and the corresponding error is not serious. On the other hand, because the large distances from the loop contain the majority of the atoms of the sum ($n \propto r^3$), the corresponding reduction in calculation time is very large, especially for large loops.

A further reduction of calculation time can, in principle, be obtained by a simultaneous calculation of interstitial and vacancy loops because in the continuum approach the displacement fields differ only in sign. However, care must be taken to consider the different stacking sequence associated with the intrinsic vacancy loop and the extrinisc interstitial loop. This yields a complex phase factor, and therefore, the imaginary part of Eqs. (2) must be calculated as well. Nevertheless, there is some calculation time saved since no additional trigonometric functions must be calculated for the vacancy loops.

C. Comparison of atomistic and continuum calculations

For small values of q a continuum approach (that is more convenient in programming) has been used for calculations along symmetry directions.[9] Because of the difficulty in estimating the systematic errors introduced by a nonatomistic sampling, we have carried out additional calculations based on a continuum approach for comparison. In the numerical integration it is important to avoid any artificial periodicity in the integration elements as they can introduce spurious maxima in reciprocal space. This was avoided here by using spherical coordinates and integration volumes that increased monotonically (but nonlinearly) with increasing r in the integration. For the individual volume elements involved in Eqs. (2), $\cos(\vec{q}\cdot\vec{r})$ was replaced by the average over the element. This is analogous to the introduction of the structure factor F_1 in the atomistic calculation and was done analytically by approximating the volume elements by spheres [$\Delta V = \frac{4}{3}\pi(\Delta r)^3$]. This yields

$$\langle \cos(\vec{q}\cdot\vec{r}) \rangle_{\Delta V} = \frac{4\pi}{q^3 \Delta V} [\sin(q\Delta r) - q\Delta r \cos(q\Delta r)] \cos(\vec{q}\cdot\vec{r}_0) .$$

Because of the more rapid convergence of the integrand of the sine transform the analogous procedure was not carried out for the sine term. For the region of $qR \lesssim 6$ this continuum approach yields very good agreement with the atomistic calculations. At large q values, however, the detailed structure of the stacking fault scattering was not fully reproduced by the continuum approximation.

IV. CHARACTERISTIC FEATURES OF THE SCATTERING FROM LOOPS

A. Typical regions in reciprocal space

To characterize the expected scattering pattern, the displacement field of a dislocation loop must be considered in some detail. For loops with $R \gtrsim 5$ Å the displacement field may be described by elastic continuum theory and after use of lattice periodicity $\vec{K}\cdot\vec{r}_m = \vec{q}\cdot\vec{r}_m$, the lattice sum in the first term of Eq. (1) may be replaced by an integral. In linear

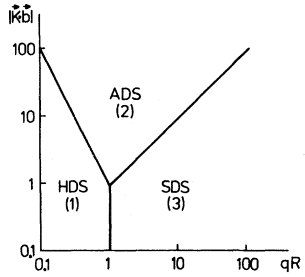

FIG. 2. Sketch of the regimes of the different types of scattering introduced in the text in a $|\vec{K}\cdot\vec{b}|$, qR plane.

elastic continuum theory the displacement field of a loop is proportional to Burger's vector b, and scales as a function f of r/R, i.e., $s \sim bf(r/R)$. Transition to the new integration variables r/R shows that the distortion-scattering (DS) intensity scales as[13]

$$I_{\mathrm{DS}} \sim R^6 F(Kb, qR) \; . \tag{3}$$

Far away from a dislocation loop, $r >> R$, the displacement field varies as $s \sim bR^2/r^2$. If, in addition $r >> R' \equiv \sqrt{Gb}\,R$, $\vec{K}\cdot\vec{s} << 1$ is obtained, and $\exp(i\vec{K}\cdot\vec{s})-1$ in Eq. (1) can be approximated by its first-order term $i\vec{K}\cdot\vec{s}$. According to reciprocity between the real and reciprocal lattice, the regime of this approximation is $qR \lesssim 1$ and $qR \lesssim 1/\sqrt{Gb}$, i.e., the immediate vicinity of the Bragg reflections as described by region 1 in Fig. 2. The scattering in this region is often called Huang diffuse scattering (HDS).

In the opposite case when $\vec{K}\cdot\vec{s} >> 1$ asymptotic approximations must be applied to obtain analytical results. The regime in reciprocal space of this approximation lies between HDS and the limits of the total distortion scattering, i.e., in $1/\sqrt{Gb} \lesssim qR \lesssim bG$ (regions 2 in Fig. 2). The scattering in this region will be called asymptotic distortion scattering (ADS) (sometimes called "Stokes-Wilson scattering"). It will be discussed later that this region is determined by differential Bragg reflections from locally distorted lattice regions.[5,6]

The region $qR \gtrsim Kb$ and $\gtrsim 1$ (regions 3 in Fig. 2) is determined by short-range disorder, i.e., by additional or missing defect atoms and their correlation with the neighboring lattice atoms (dislocation core, stacking fault). The scattering in this region can be understood as Laue scattering from the defect atoms and its interference with distortion scattering. It will be called structural diffuse scattering (SDS).

The most important consequence of Eq. (3) for practical applications is the possibility of scaling the intensities for different loop sizes: as long as the diffuse-scattering intensity is dominated by the distortion scattering (regions 1 and 2 of Fig. 2), the intensity distributions for loops of different radii can be obtained directly from that, for one certain radius by scaling according to Eq. (3). This conclusion has been tested and confirmed by the numerical calculations.

B. Huang diffuse scattering

The scattering in the immediate vicinity of the Bragg reflections $qR' < 1$ is determined by the small displacements of the long-range part of the displacement field. Thus, the scattering intensity, Eq. (1), becomes

$$I_{\mathrm{HDS}} = |\vec{G}\cdot\vec{s}^{\,*}(\vec{q})|^2 \; . \tag{4}$$

Two important features of this expression are easily obtained.[6] From $s \sim bR^2/r^2$ it follows that $s^* \sim bR^2/(vq)$ and

$$I_{\mathrm{HDS}} \sim (GbR^2)^2/(vq)^2 \; ;$$

thus, the intensity increases as $1/q^2$ when approaching a reciprocal-lattice point.[3,4] From the inversion symmetry $\vec{s}(\vec{r}) = -\vec{s}(-\vec{r})$ it follows that $\vec{G}\cdot\vec{s}^{\,*}(\vec{q}) = -\vec{G}\cdot\vec{s}^{\,*}(-\vec{q})$ must change sign and thus I_{HDS} must vanish on at least one surface passing through the reciprocal-lattice point $\vec{G}$. Since I_{HDS} is "homogeneous" ($\propto 1/q^2$) in $\vec{q}$, such a nodal surface is generated by straight lines through $\vec{q}=0$.

Because measured intensities usually consist of the contributions from several equivalent defect configurations, the $I_{\mathrm{HDS}}=0$ surface of a certain configuration may be masked by the intensity from other configurations. From remaining surfaces or lines of vanishing intensity, conclusions on the symmetry of the defects can be drawn, as has been shown earlier.[3]

In order to get more detailed features of Huang scattering from dislocation loops we express their displacement field $\vec{s}(\vec{r})$ via the elastic Green's function $G(r)$ and the force array $\vec{f}(\vec{r})$ describing the loop. Fourier transformed, this relation is[3]

$$\vec{s}^{\,*}(\vec{q}) = G^*(\vec{q})\cdot\vec{f}^{\,*}(\vec{q}) \; , \tag{5a}$$

where $G^*(q)$ satisfies the Fourier-transformed equilibrium condition

$$\sum_{klm} G^*_{ik} C_{klmn} q_1 q_m = \delta_{in} \tag{5b}$$

with the elastic constants C_{klmn} and

$$f^*_k(\vec{q}) = i \sum_{lmn} C_{klmn} q_l b_n \int dA_m e^{i\vec{q}\cdot\vec{r}} \; . \tag{5c}$$

For $qR' << 1$ the integral over the loop area A becomes identical with A.

In the case of elastic isotropy a general statement can be made on the number of nodal surfaces at which $\vec{G}\cdot\vec{s}^{\,*}(\vec{q}) = 0$ and hence $I_{\mathrm{HDS}}(\vec{q})=0$. Then, $\vec{s}^{\,*}(\vec{q})$ is of the cubic form $q_i q_j q_k/q^4$ as a result of a product of terms $q_i q_j/q^2$ and q_k arising from the elastic Green's function and the force array, respectively. Hence, due to the cubic form in a plane in reciprocal space, $\vec{G}\cdot\vec{s}^{\,*}(\vec{q})=0$ has three

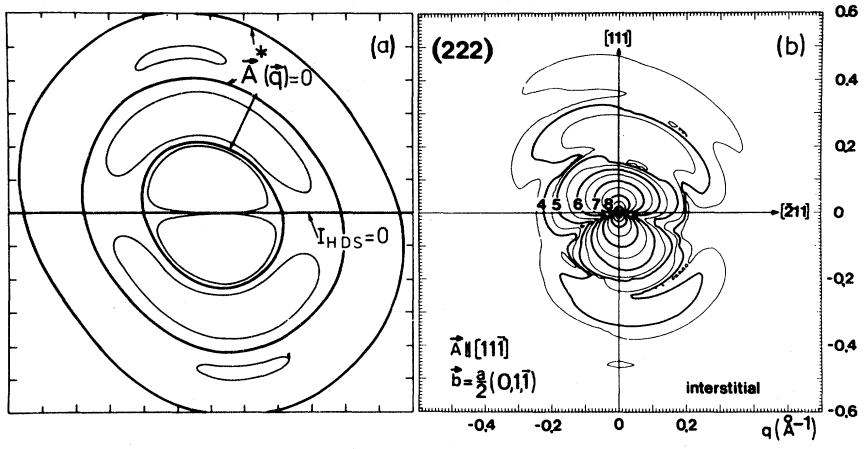

FIG. 3. Scattering from a dislocation loop with $\vec{A}$ paralled to $[11\bar{1}]$ and $\vec{b}=(a/2)\,(0,1,\bar{1})$. Isointensity lines are shown for the region close to the (222) reflection in the $(01\bar{1})$ plane of the reciprocal lattice. (a) $|G\cdot s^*(\vec{q})|^2$, the nodal lines (thick) have been calculated analytically, and (b) numerically calculated isointensity lines for a $R=20$-Å loop. The numbers give the intensity in a logarithmic scale.

solutions (one or three *real* solutions) describing straight lines through $\vec{q}=0$. In the case of elastic anisotropy additional solutions can exist.

For special cases one of the solutions can become very simple. Thus if

$$\vec{G}\cdot\vec{b}=0,\quad I_{\mathrm{HDS}}=0 \quad \text{for } \vec{q}\,||\,\vec{A}\,, \tag{6a}$$

if

$$\vec{G}\cdot\vec{A}=0,\quad I_{\mathrm{HDS}}=0 \quad \text{for } \vec{q}\,||\,\vec{b}\,, \tag{6b}$$

since for $\vec{q}\,||\,\vec{A}$, i.e., for $A_m=Aq_m/q$, Eq. (5a) yields with (5b) and (5c):

$$\vec{s}^*(\vec{q}\,||\,\vec{A})=i\vec{b}A/q \quad \text{for } qR<<1\,,$$

and analogously for $\vec{q}\,||\,\vec{b}$,

$$\vec{s}^*(\vec{q}\,||\,\vec{b})=i\vec{A}b/q \quad \text{for } qR<<1\,.$$

These nodal lines of HDS are shown in Figs. 3 and 4 which are described in more detail in the next section.

C. Scattering for $\vec{K}\vec{b}<<1$

If $\vec{K}\cdot\vec{b}<<1$ the expansion of $\exp(i\vec{K}\cdot\vec{s})$ up to the linear term is also valid for $qR>1$. However, in this case the "form factor" of the loop $\int d\vec{A}\,e^{i\vec{q}\cdot\vec{r}}$, appearing in both the distortion and the Laue term, has to be considered: for the case of a circular loop

$$\vec{A}^*(\vec{q})=\int d\vec{A}\,e^{i\vec{q}\cdot\vec{r}}$$
$$=2\vec{A}J_1(q_AR)/(q_AR)\,, \tag{7}$$

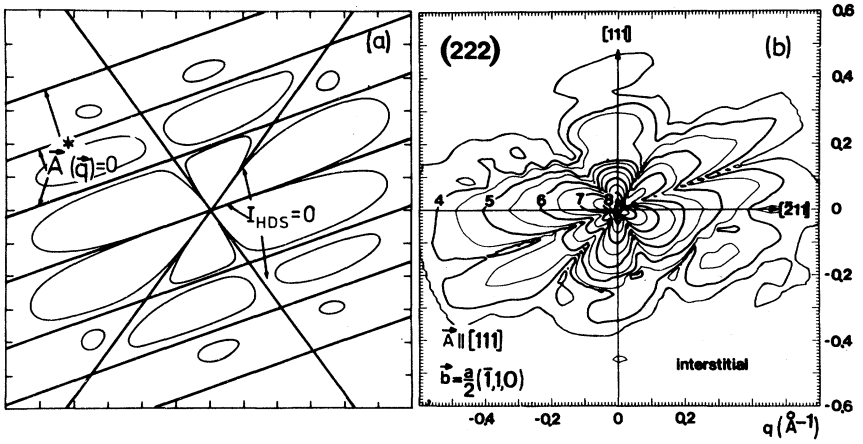

FIG. 4. Isointensity lines as in Fig. 3 for a loop with $\vec{A}$ parallel to $[\bar{1}11]$ and $\vec{b}=(a/2)(\bar{1},1,0)$.

where J_1 is the first-order Bessel function, and

$$q_A=[q^2-(\vec{q}\vec{A})^2/A^2]^{1/2}$$

results from the projection $\vec{q}$ on $\vec{A}$. Hence, in addition to the zeros of I due to the long-range part of $\vec{s}(\vec{r})$, as discussed in the previous section, zeros due to the loop structure appear. For circular loops they are cylinders perpendicular to the loop area and with radii determined by the zeros of J_1.

The characteristics of the scattering pattern are essentially determined by the nodal surfaces in reciprocal lattice as is demonstrated in Figs. 3 and 4. These figures show the nodal lines [Figs. 3(a) and 4(a)] and the numerically calculated isointensity lines [Figs. 3(b) and 4(b)]. The nodal lines passing through the origin are due to $I_{\mathrm{HDS}}=0$ while the other ones are due to $\vec{A}^*(\vec{q})=0$. In spite of the finite numerical resolution, the zero intensity lines shown in Figs. 3(a) and 4(a) are all reproduced by the isointensity lines, in Figs. 3(b) and 4(b).

In the region of small-angle scattering $\vec{K}=\vec{q}$, the Laue term can no longer be neglected:

$$I\approx\frac{1}{v^2}\,|\,i\vec{q}\cdot\vec{s}^*(\vec{q})+\vec{b}\vec{A}^*(\vec{q}\,|\,^2\,. \tag{8a}$$

With the use of Eq. (5a)–(5c), and the Lagrange identity

$$(\vec{a}\times\vec{b})\cdot(\vec{c}\times\vec{d})=(\vec{a}\cdot\vec{c})(\vec{b}\cdot\vec{d})-(\vec{b}\cdot\vec{c})(\vec{a}\cdot\vec{d})$$

for the vector product, this can be written as[14]

$$I=\frac{1}{v^2}\,|\,[\vec{q}\times(\vec{b}-\vec{b}')]\cdot[\vec{q}\times\vec{A}^*(\vec{q})]/q^2\,|\,^2\,, \tag{8b}$$

with

$$b'_m=\sum_{jkln}q_jG_{jk}C_{klmn}q_1b_n,\quad \vec{b}'\cdot\vec{q}=\vec{b}\cdot\vec{q}$$

which shows clearly that $I=0$ for $\vec{q}\,||\,\vec{A}$ (see also Fig. 10 below).

D. Asymptotic distortion scattering

If $\vec{G}\vec{b}>>1$, the contributions to the scattering amplitude from the region $r<(\vec{G}\cdot\vec{b})^{1/2}R$ are rapidly oscillating in $\vec{r}$ and essentially cancel each other. Relevant contributions come only from those positions $\vec{r}=\vec{r}_s$ where the phase $\varphi=\vec{q}\cdot\vec{r}+\vec{K}\cdot\vec{s}$ becomes stationary[6]

$$\nabla\varphi=\vec{q}+\vec{\nabla}(\vec{K}\cdot\vec{s})=0\quad\text{for }\vec{r}=\vec{r}_s\,. \tag{9}$$

Expansion of the phase according to the method of stationary phase up to second-order terms yields an amplitude

$$A=\frac{(2\pi)^{3/2}}{v}\sum_{\vec{r}_s}\exp[i\varphi(\vec{r}_s)+i\tfrac{1}{4}\pi\sigma(\vec{r}_s)]/[D(\vec{r}_s)]^{1/2}\,, \tag{10}$$

where $\sigma(\vec{r})$ is the difference between the number of positive and that of negative eigenvalues of $(\partial/\partial x_i)(\partial/\partial x_j)(\vec{K}\cdot\vec{s})$, and $D(\vec{r})$ is its determinant

$$D(\vec{r})=\det\left[\frac{\partial}{\partial x_i}\frac{\partial}{\partial x_j}(\vec{K}\cdot\vec{s})\right].$$

Equation (9) induces a point-to-point mapping from the real into the reciprocal lattice. It can be interpreted as the Bragg condition for locally deformed regions (local Bragg reflection). For instance, compressed regions (strain $\epsilon<1$) scatter on the opposite side of $\vec{G}$ from expanded regions (strain $\epsilon>1$) as indicated schematically in Fig. 5. Neglecting the oscillations described by the phase factor in (10) we get for the intensity

$$I_{\mathrm{ADS}}\sim\frac{1}{v^2}\sum_{\vec{r}_s}\frac{1}{D(\vec{r}_s)}\,. \tag{11}$$

Thus the intensity is given by the density of local Bragg reflections. For the long-range displacement field of a dislocation loop $s\sim bR^2/r^2$, this becomes with

$$D(r_s)\sim(KbR^2)/r_s^4)^3$$

and $q\sim KbR^2/r_s^3$,

$$I_{\mathrm{ADS}}\sim KbR^2/(v^2q^4)\,, \tag{12}$$

a general trend which is confirmed by the numerical calculations.

E. Oscillations in the scattering pattern

Owing to inversion symmetry $\vec{s}(\vec{r})=-\vec{s}(-\vec{r})$ there are (always) at least two points of the real lattice "scattering" into one point of the reciprocal lattice. This interference between local Bragg reflections leads to oscillations in the scattering pattern occurring at one side of the reciprocal-lattice point as depicted in Fig. 5. For the long-range displacement field $s\sim bR^2/r^2$ the phase goes as[15]

$$\varphi(\vec{r}_s)=\vec{q}\cdot\vec{r}_s+\vec{K}\cdot\vec{s}(\vec{r}_s)\sim(KbR^2q^2)^{1/3}\,. \tag{13}$$

Of course, the behavior is strongly constricted by the limits of both types of asymptotic approximations, the one for the displacement field and the

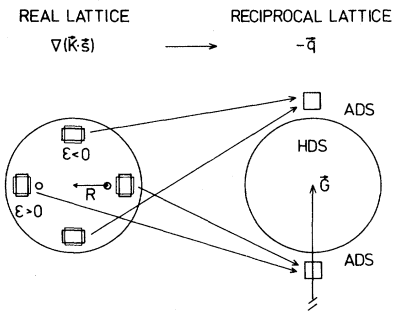

FIG. 5. Mapping from the real into the reciprocal lattice. The distortion in the real lattice is indicated by rectangular figures; ϵ is the strain along the direction of $\vec{G}$.

one for the distortion scattering, i.e.,

$$\frac{1}{\sqrt{Gb}} \lesssim qR \lesssim 1 .$$

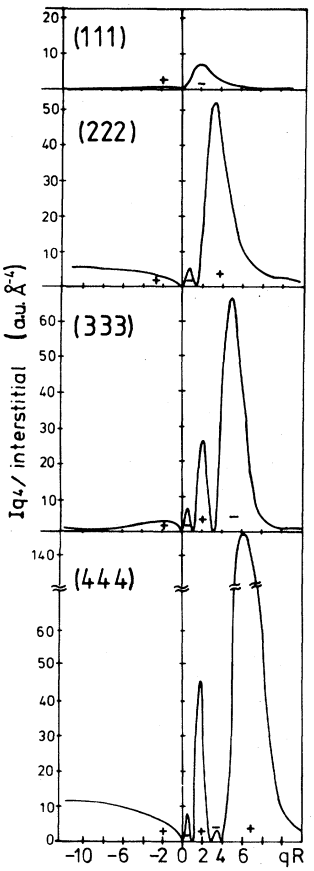

FIG. 6. Oscillations of the scattering intensity from a loop $\vec{A}$ parallel to [111], $\vec{b}=(a/3)(1,1,1)$ at (111), (222), (333), and (444) reflections. To demonstrate that the intensity has zeros the changing signs of the scattering amplitudes are shown for the different regions. The oscillations scale with the loop size according to Eq. (3).

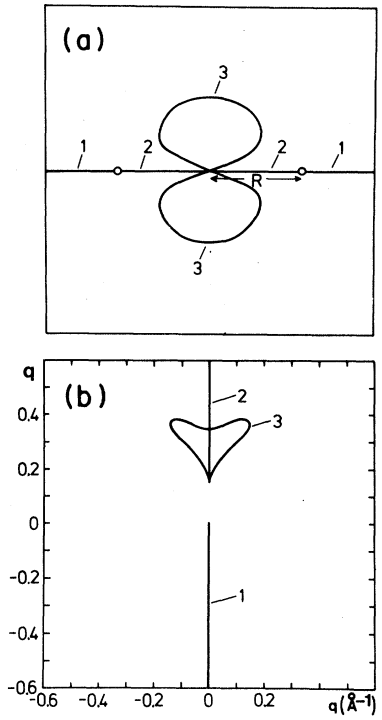

FIG. 7. Lines of "stationary strain" (a), for a loop with $\vec{A}$ parallel to [111], $\vec{b}=(a/3)$ (1,1,1), and the corresponding "caustics" (b) at the (444) reflection.

The number of maxima within this region can be estimated by considering the change of the phase $\varphi(\vec{r}_{\vec{s}})$. It increases from 0 for $r\to\infty$ ($q=0$) to $\vec{G}\cdot\vec{b}/2$ in the center of the loop. In a plot of Iq^4 [which best shows the oscillations for the q^{-4} fall off of $I(\vec{q})$] this will result in

$$n=(\vec{G}\cdot\vec{b})/2\pi \tag{14}$$

maxima. This is borne out clearly by the calculation for loops with $\vec{A}\|[111]$, $\vec{b}=\frac{1}{3}a(1,1,1)$ and $\vec{q}$ along [111] for four orders of the (hhh) reflection in Fig. 6. In contrast to these oscillations along the [111] direction there is no structure along $[\bar{1}\bar{1}\bar{1}]$ because the spatial separation of points contributing to scattering on this side of $\vec{G}$ has no projection on $\vec{G}$ (see Fig. 5).

F. Caustics

According to the picture of Bragg reflections from locally deformed parts of the lattice, strong intensity contributions may be expected from regions where the relevant deformation $\nabla(\vec{K}\cdot\vec{s})$ is slowly varying and, in particular, where it has an extremum. Thus high intensity should come from the equatorial plane of a loop and especially high intensity can be expected from its center (see Fig. 7).

In fact, at those surfaces $D(\vec{r}_s)=0$, i.e., the density of local Bragg reflections becomes infinite, $I\to\infty$. In optics such surfaces are known as caustics. Caustics define the bifurcation set for the mapping from the real into the reciprocal lattice. Here at least two stationary points coalesce and higher-order terms in the expansion of the phase φ must be considered in the asymptotic approximation.[16]

Again, for the case of inversion symmetry $\vec{s}(\vec{r})=-\vec{s}(-\vec{r})$, it follows from $D(\vec{r})=-D(-\vec{r})$ that $D(\vec{r})=0$ has real solutions, i.e., that caustics must exist. In the case of rotational symmetry, as shown in Fig. 7, ring-shaped regions in the equatorial plane of the loop "scatter" into single points in reciprocal lattice (caustic 1). For $s\sim bR^2/r^2$, integration over the rings gives

$$I\sim(KbR^2)^{4/3}/(v^2q^{10/3})$$

close to the Huang region and

$$I\sim(KbR)^2/(v^2q^4)$$

further away. For the center of the loop where $qR\sim Kb$, expansion of the phase up to third-order terms yields $I\sim R^6/(vKb)^2$ (caustics 2 and 3).

Of course, even for the highest order of reflection which can be investigated the extreme asymptotic region characterized by strongly pronounced caustics is never reached. However, even in the intermediate case, one can say that the caustics form the "skeleton" of the scattering pattern. For individual loops with $\vec{K}\cdot\vec{b}\gtrsim 1$ (see Fig. 8) the "backbone" (caustic 1) and the "skull" with its "horn" (caustics 2 and 3) can clearly be recognized.

The position of the final peak of the distortion scattering related to caustics 2 and 3 lies close to the local Bragg reflection due to the center of the loop $\vec{q}_c=-\nabla(\vec{G}\cdot\vec{s})_c$ and the Bragg reflection due to the average strain within a sphere including the loop $\langle\vec{q}\rangle=-\langle\nabla(\vec{G}\cdot\vec{s})\rangle$. Both positions are introduced in Figs. 10 and 12.

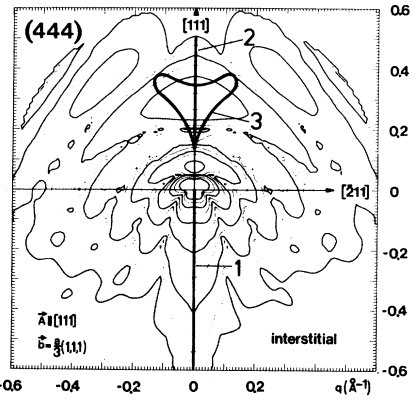

FIG. 8. Caustics as the skeleton of the scattering pattern for large $\vec{b}\cdot\vec{G}$ shown close to the (444) reflection, for a loop with $\vec{A}$ paralled to [111] and $\vec{b}=(a/3)(1,1,1)$.

G. Stacking fault scattering

Planar discontinuities of the displacement field as well as added (or removed) lattice planes (the source of the displacement field) yield intensity streaks perpendicular to these planes. In the case of perfect loops these types of contributions cancel each other as can be seen from Fig. 9. The reason for this is that the region surrounded by the dislocation loop has a continuously disturbed lattice structure and that for infinitely large perfect loops diffuse scattering at a certain finite $\vec{q}$ must vanish asymptotically. This fact can be used to separate stacking fault scattering from other types of contributions: Faulted loops are considered to be generated from perfect loops by specific shear displacements.

For randomly distributed loops, the scattering from individual loops can be added incoherently in contrast to the case of cold worked materials for

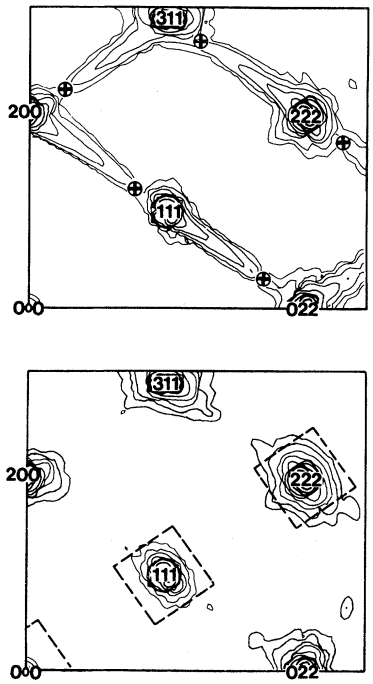

FIG. 9. General features of the scattering pattern in the $(01\bar{1})$ plane of the reciprocal lattice. Isointensity curves are shown for interstitial loops on all {111} planes: upper part for Frank or faulted loops and lower part for perfect loops.

which, in general, long-range correlations between stacking faults are important.

The scattering contribution due to the stacking fault of a crystal can be separated from the other contributions by a rearrangement of the lattice sums (corresponding to partial integration for integrals) and extraction of the terms describing the discontinuities. Let $F(\vec{K})$ be the structure amplitude of a stacking plane, $T_m = F(\vec{K})\exp(\vec{K}\cdot\vec{r}_m)$ be the scattering amplitude of a stacking plane m in the unfaulted crystal, and S_m the phase factor describing its transversal position in the faulted crystal (shear factor). Then the scattering amplitude A of a crystal with N stacking planes may be written as

$$A = \sum_{m=1}^{N} S_m T_m = +S_N \sum_{m=1}^{N} T_m - \left[\sum_{m=1}^{N-1} (S_{m+1} - S_m) \sum_{h=1}^{m} T_n \right] . \tag{15}$$

For a dislocation loop of radius R the sum is thought to be carried out over a cylinder with radius R and height $h \approx R$ (h need not be specified precisely since we will find that it drops out in the stacking fault scattering).

The first term in (15) describes the Bragg amplitude A_B due to the unfaulted crystal, the second one the amplitude A_s due to the stacking fault. For a single stacking fault the shear factor S_m differs only for some, for example, z, pairs of neighboring planes at $m \geq L$ ($z = 1$ for an intrinsic stacking fault, $z = 2$ for an extrinsic stacking fault):

$$S_{m+1} - S_m = 0$$

for

$$m < L \text{ and } m > L + z - 1 .$$

Extracting the stacking fault term we get a scattering amplitude

$$A_s = -\sum_{m=L}^{L=z-1} (S_{m+1} - S_m) \sum_{n=1}^{m} T_n = F(\vec{K}) \frac{\left[S_{L+z} - S_L - e^{i\vec{K}\cdot\vec{r}_0 L} \sum_{m=0}^{z-1} (S_{L+m+1} - S_{L+m}) e^{i\vec{K}\cdot\vec{r}_0 m} \right]}{(1 - e^{-i\vec{K}\cdot\vec{r}_0})} , \tag{16}$$

where $\vec{r}_0$ is a lattice vector connecting two neighboring stacking planes. Averaging the corresponding intensity $I_s = \langle |A_s|^2 \rangle$ over $\Delta\vec{K}\cdot\vec{r}_0 L >> 1$ yields

$$I_s = |F(\vec{K})|^2 \frac{\left[\left| S_{L+z} - S_L \right|^2 + \left| \sum_{m=0}^{z-1} (S_{L+m+1} - S_{L+m}) e^{i\vec{K}\cdot\vec{r}_0} \right|^2 \right]}{[4\sin^2(\vec{K}\cdot\vec{r}_0/2)]} . \tag{17}$$

Application to faulted vacancy loops (intrinsic stacking fault) yields

$$I_s = 2F(\vec{K})^2 \frac{\sin^2(\vec{K}\cdot\vec{s}/2)}{\sin^2(\vec{K}\cdot\vec{r}_0/2)} , \tag{18}$$

where $\vec{s}$ is the shear displacement generating the stacking fault.

For interstitial loops (extrinsic stacking fault) the scattering intensity is

$$I_s = |F(\vec{K})|^2 \frac{\sin^2(\vec{K}\cdot\vec{s}) + 4\sin^2(\vec{K}\cdot\vec{s}/2)\cos^2(\vec{K}\cdot\vec{r}_0/2 + \vec{K}\cdot\vec{s}/2)}{\sin^2(\vec{K}\cdot\vec{r}_0/2)} , \tag{19}$$

where now $\vec{s}$ is the shear displacement of the upper lattice planes with respect to the loop plane. The cosine term describing the interference between the two shear displacements necessary for extrinsic loops yields nodal points in the streak pattern at 0.273 of the distance between two reflections as shown in Fig. 9. This property can, in principle, be used to separate faulted interstitial and vacancy loops.

The structure factor gives the width $\delta q \approx 1/R$ of the stacking fault streaks yielding the size of the loops whereas their maximum intensity ($\propto R^4$) provides the fourth moment of the size distribution.

V. RESULTS FOR LOOPS ON {111} PLANES IN fcc LATTICES

In this section, the intensity contours for dislocation loops on {111} planes are discussed in detail. In addition to contours for selected loop orientations, contours are shown for the average over loops on all cubic equivalent planes, which is the usual situation experimentally.

A. Symmetry of loops on {111} planes in cubic lattices

With a statistical distribution of loops in a single crystal we have to consider the four equivalent {111} planes. This yields four different Frank loops (of $\frac{1}{3}a(1,1,1)$-type Burgers vector) and twelve different perfect loops (of $\frac{1}{2}a(1,1,0)$-type Burgers vector). Because of the translation symmetry of the lattice, loops of *A*, *B*, or *C* type are equivalent. As the direction of the stacking sequence *A*, *B*, and *C* of the lattice is well defined, there are in a given crystal no possibilities of different stacking directions, as was discussed for basal loops in hcp crystals[8] (*AB* or *BA* loops).

If the intensity is considered on symmetry planes in reciprocal space, the number of different loop orientations to be calculated is reduced. For the $(01\bar{1})$ plane considered below, the loops to be calculated are shown in Table I (together with the weighting factor, the different loops get in the averaging). For calculations around a high symmetry reflection, e.g., of $(h00)$ type, the actual number of calculated loops can obviously be reduced by a mirror operation.

B. Intensity contours

Isointensity contours for 20-Å loops on {111} planes of both Frank $[\vec{b}=\frac{1}{3}a(1,1,1)]$ and perfect $[\vec{b}=\frac{1}{2}a(1,1,0)]$ nature are shown in Fig. 9. This figure gives an overall view of the scattering in the $(01\bar{1})$ plane of reciprocal space. Figure 9(a) represents the scattering for Frank loops and contains intense scattering streaks along all [111] directions except the radial direction from the origin. These streaks are due to scattering from the stacking fault associated with Frank-type loops as discussed in Sec. IV G. The scattering from unfaulted (perfect) loops [Fig. 9(b)] contains no such scattering streaks. The scattering close to reciprocal-lattice points will be shown below in an enlarged scale for the regions around (hhh)-type reflections indicated in Fig. 9(b). The crossed circles in Fig. 9(a) represent the positions of nodes in the stacking fault scattering predicted by Eq. (19). It can be seen that minima remain at these positions even when the scattering is averaged over all {111} loop orientations. Calculations for vacancy loops (not shown) of faulted and perfect types indicate qualitatively similar results, except that the nodes (or minima) in the stacking fault scattering do not appear for the intrinsic stacking fault case [Eq. (18)].

Figure 10 shows intensity contours for Frank loops in the vicinity of the (000), (111), and (222) reciprocal-lattice points in more detail. Column 1 contains the scattering from only the loop with $\vec{A}\|[111]$, and columns 2 and 3 contain the scattering for the $\vec{A}\|[11\bar{1}]$ and $\vec{A}\|[\bar{1}11]$ loop, respective-

TABLE I. Loops to be considered for the scattering in the $(01\bar{1})$ plane of reciprocal lattice.

		Perfect loop			Faulted loop		
Nr	$\vec{A}$	$\vec{b}$	Weight	Remark	$\vec{b}$	Weight	Remark
1*a*	(111)	⟨110⟩	2		⟨111⟩	1	
b	(111)	⟨011⟩	1				
c	(111)	⟨101⟩		*id*,1*a*			
2*a*	$(11\bar{1})$	⟨110⟩	2		$\langle 11\bar{1}\rangle$	2	
b	$(11\bar{1})$	$\langle 01\bar{1}\rangle$	2				
c	$(11\bar{1})$	$\langle 10\bar{1}\rangle$	2				
3*a*	$(1\bar{1}1)$	$\langle 1\bar{1}0\rangle$		*id*,2*c*	$\langle 1\bar{1}1\rangle$		*id*,2*a*
b	$(1\bar{1}1)$	$\langle 0\bar{1}1\rangle$		*id*,2*b*			
c	$(1\bar{1}1)$	⟨101⟩		*id*,2*a*			
4*a*	$(\bar{1}11)$	$\langle \bar{1}10\rangle$	2		$\langle \bar{1}11\rangle$	1	
b	$(\bar{1}11)$	⟨011⟩	1				
c	$(\bar{1}11)$	$\langle \bar{1}01\rangle$		*id*,4*a*			

ly. Figure 11 contains the average scattering (see Table I) from all four loop orientations, as was presented in Fig. 9(a). For the case of the (000) reflections (which corresponds to small-angle scattering) the zero intensity line along $\vec{q}||\vec{A}$ is obtained for the individual loops (columns 1 and 3 of Fig. 10), but the superposition of scattering in the averaging over the $\{111\}$ orientations gives rise to an essentially isotropic scattering pattern, as shown in Fig. 11. Although the scale of Figs. 10 and 11 is too large to distinguish details in the HDS at very small q, the features of the ADS and SDS can be clearly identified at both the (111) and (222) reflections. A satellite is apparent in the (222)-reflection case for $\vec{A}||[111]$ (as discussed in connection with Figs. 6 and 8), and both the stacking fault scattering and their minima are observable in column 3. The averaged intensity for both the (111) and (222) cases retains the identity of the stacking fault scattering, but much of the other

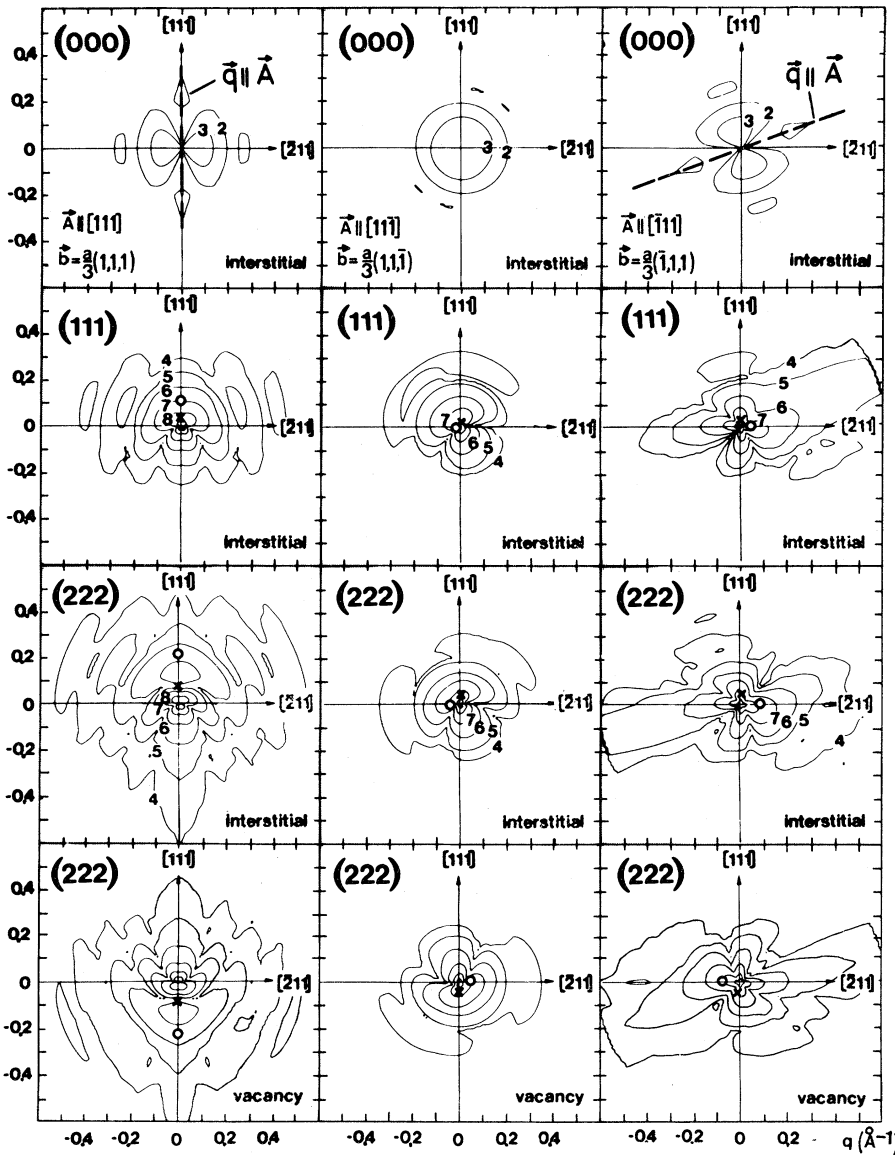

FIG. 10. Scattering intensities for the different orientations of Frank loops (see Table I). Isointensity plots are shown for the regions close to (000), (111), and (222) reflections in the $(01\bar{1})$ plane of the reciprocal lattice. Calculations for a $R=20$-Å loop; intensities are given in a logarithmic scale. The positions of the local reflections due to the strain at the center of the loops (x), and due to the average strain within a sphere including the loops (o), respectively, are introduced.

scattering. The asymmetry in the scattering for $\vec{q}$ parallel and $\vec{q}$ antiparallel to $\vec{G}$, even after averaging, makes it possible to distinguish vacancy from interstitial loops with confidence. The result gives more quantitative proof for the interpretation of earlier experimental observations at low-temperature irradiated Cu (Ref. 17) and Au (Ref. 18) where a large change in this asymmetry was observed during annealing stage III, when vacancy agglomerates are formed in addition to the preexisting interstitial loops.

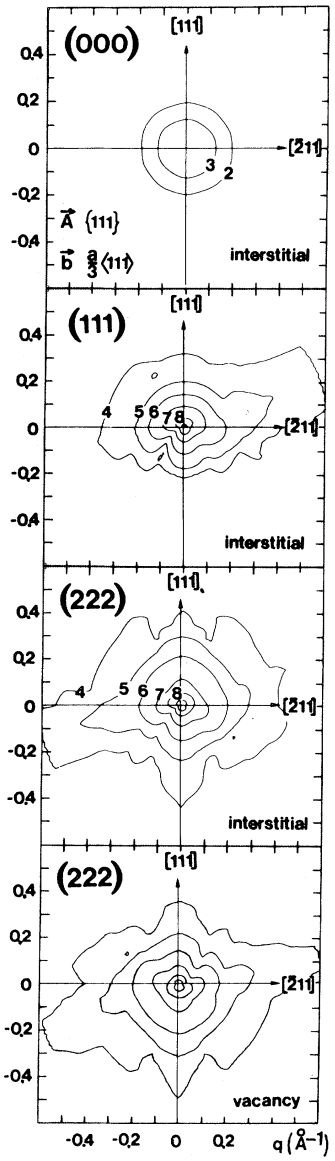

FIG. 11. Average intensities of the different Frank loops shown in Fig. 10.

The scattering from perfect dislocation loops is shown in Fig. 12 for the (222) reflection. Only two examples of the intensities of the seven different loop types are shown in the figures together with the average intensity (see Table I). Loop 1(a) looks, except for some distortion, very similar to the corresponding Frank loop with $\vec{A}$ parallel to $\vec{G}$. As the intensity in this situation is determined by the projection of $\vec{s}$ on $\vec{G}$ there are also only minor differences to loop 1(b), (not shown) that has the same habit plane but a Burgers vector lying within the $(01\bar{1})$ plane of the figure. A typical representative of the loops of types 2 and 3 was shown in Fig. 3; the others also show no prominent structure. The loops of type 4 (the normal of A in the measuring plane but not parallel to $\vec{G}$) look quite different depending on the direction of $\vec{b}$. For $\vec{b}$ outside the $(01\bar{1})$ plane the scattering has been shown in Fig. 4. The loop 4*b* [with $\vec{b}$ in the $(01\bar{1})$ plane] is shown in Fig. 12; it is characterized by a strong intensity peak in the direction of the loop normal.

Except for the missing stacking fault scattering the average intensity is qualitatively very similar to that for the Frank loops in Fig. 11. For this case, there is an even better mirror symmetry between vacancy and interstitial loops. The similarity in the scattering from Frank and perfect loops for $q \lesssim 0.3$ Å^{-1} renders this lower-q region rather insensitive to the faulted or unfaulted nature of vacancy or interstitial loops; on the other hand, this fact does allow size determinations of vacancy and intersititial loops independent of the presence (or absence) of stacking faults.

Although the intensity oscillations arising from the $\vec{A}||[111]$ loop for the (222) reflections in Figs. 10 and 12 are not resolved in the averaged intensity plots in these figures, plots of q^4I do show well-resolved peaks which have been observed experimentally.[19] The position of these peaks can be used as a direct estimate of the loop sizes and vacancy-interstitial nature, as discussed above. When distributions of sizes are present, a fitting procedure can be used to determine the dislocation loop density and size distribution.

SUMMARY AND CONCLUSIONS

The problem of long computation time associated with numerical calculations of diffuse scattering

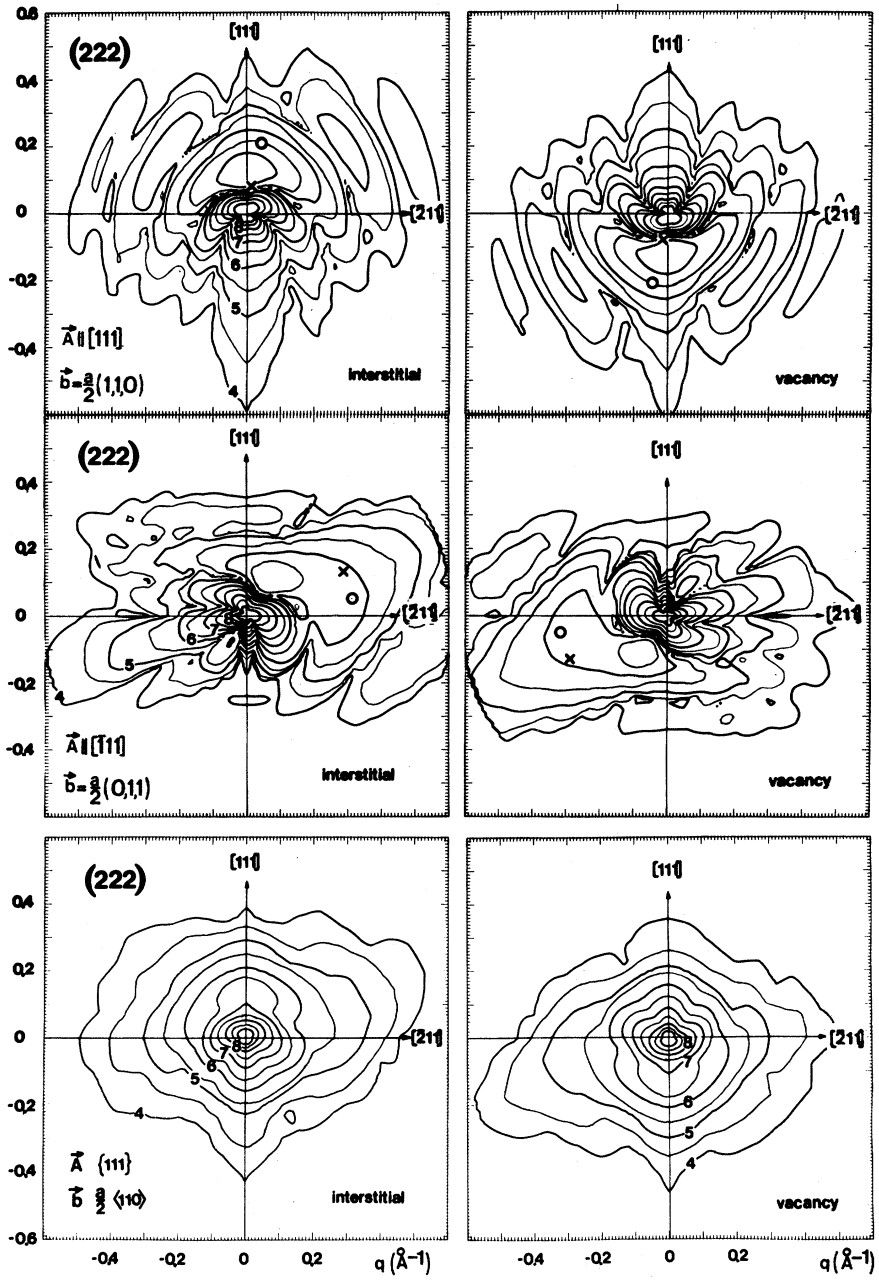

FIG. 12. Isointensity curves similar to Figs. 10 and 11 for two different perfect loops of interstitial and vacancy type and for the average over all possible loop orientations (see Table I). Positions (x) and (o) as in Fig. 10.

from dislocation loops has been addressed through the use of a Gaussian damping function to reduce the size of the integration volumes required. In addition, summing procedures were introduced to combine the scattering of groups of atoms into a single structure factor in order to preserve the atomistic nature of the calculation while using larger differential volume elements in the integration. These approaches have made the calculation of the scattering from loops to $R \approx 100$ Å tractable.

Further, the application of new analytical approaches as guides throughout the investigation have provided a better fundamental understanding of the features of the scattering distributions, have provided insight into the selection of the appropriate expressions for numerical computation in the

various scattering regimes, and have helped to reduce the possibilities for numerical errors.

Characteristic differences in the scattering from faulted and perfect dislocation loops, and differences between the scattering from vacancy type and interstitial type loops have been demonstrated, which provide a sound basis for an experimental discrimination between these loop types. Absolute intensities of the scattering can be used for the determination of the concentration and size of the dislocation loops. It must be borne in mind, however, that the dislocation loops are assumed to be randomly distributed (no correlations between loops) and they are not intersecting to form dislocation networks rather than individual loops.

The authors acknowledge helpful discussions with Dr. S. M. Ohr on the calculation of displacement fields.

---

*Work performed in part while a guest in the Solid State Division, Oak Ridge National Laboratory, Oak Ridge, Tennessee.

[1]P. Ehrhart, J. Nucl. Mater. 69/70, 200 (1978).

[2]B. C. Larson, in *Proceedings of the Conference on Fundamental Aspects of Radiation Damage in Metals,* edited M. T. Robinson and F. W. Young Jr., U.S. ERDA Conference Nos. 751006-*P*2, Oak Ridge, Tennessee (1976).

[3]H. Trinkaus, Phys. Status Solidi B 51, 307 (1972); 54, 209 (1972).

[4]P. H. Dederichs, Phys. Rev. B 4, 1041 (1971).

[5]P. H. Dederichs, J. Phys. F 3, 471 (1973).

[6]H. Trinkaus, Z. Ang. Phys. 31, 229 (1971); Z. Naturforsch. 28a, 980 (1973).

[7]M. A. Krivoglaz, *Theory of X-Ray and Thermal Neutron Scattering by Real Crystals* (Plenum, New York, 1969).

[8]D. T. Keating and A. N. Goland, Phys. Rev. B 4, 1816 (1971); B 10, 2232 (1974).

[9]B. C. Larson and W. Schmatz, Phys. Status Solidi B 99, 267 (1980).

[10]S. M. Ohr, Phys. Status Solidi B 64, 317 (1974).

[11]D. T. Keating and A. N. Goland, Acta Crystallogr A27, 134 (1971).

[12]E. Eisenriegler, Cryst. Lattice Defects 2, 181 (1971).

[13]P. H. Dederichs, Phys. Rev. B 1, 1306 (1969).

[14]A. Seeger and E. Kröner, Z. Naturforsch. Teil A 14, 74 (1959).

[15]H. Trinkaus, H. Peisl, and H. Spalt, Phys. Status Solidi A 2, K97.

[16]H. Trinkaus and F. Drepper, J. Phys. A 10, L11 (1977).

[17]P. Ehrhart and U. Schlagheck, J. Phys. F 4, 1589 (1974).

[18]E. Segura and P. Ehrhart, Radiat. Eff. 42, 233 (1979).

[19]P. Ehrhart and U. Schlagheck, Ref. 2, p. 839.